

Article

Au/ZnO Hybrid Nanostructures on Electrospun Polymeric Mats for Improved Photocatalytic Degradation of Organic Pollutants

Laura Campagnolo ^{1,2}, Simone Lauciello ³, Athanassia Athanassiou ¹  and Despina Fragouli ^{1,*} 

¹ Smart Materials, Istituto Italiano di Tecnologia, Via Morego 30, 16163 Genova, Italy

² Dipartimento di Chimica e Chimica Industriale, Università degli Studi di Genova, Via Balbi 5, 16126 Genova, Italy

³ Electron Microscopy Facility, Istituto Italiano di Tecnologia, Via Morego 30, 16163 Genova, Italy

* Correspondence: despina.fragouli@iit.it; Tel.: +39-010-289-6878

Received: 31 July 2019; Accepted: 22 August 2019; Published: 28 August 2019



Abstract: An innovative approach for the fabrication of hybrid photocatalysts on a solid porous polymeric system for the heterogeneous photocatalytic degradation of organic pollutants is herein presented. Specifically, gold/zinc oxide (Au/ZnO)-based porous nanocomposites are formed in situ by a two-step process. In the first step, branched ZnO nanostructures fixed on poly(methyl methacrylate) (PMMA) fibers are obtained upon the thermal conversion of zinc acetate-loaded PMMA electrospun mats. Subsequently, Au nanoparticles (NPs) are directly formed on the surface of the ZnO through an adsorption dipping process and thermal treatment. The effect of different concentrations of the Au ion solutions to the formation of Au/ZnO hybrids is investigated, proving that for 1 wt % of Au NPs with respect to the composite there is an effective metal–semiconductor interfacial interaction. As a result, a significant improvement of the photocatalytic performance of the ZnO/PMMA electrospun nanocomposite for the degradation of methylene blue (MB) and bisphenol A (BPA) under UV light is observed. Therefore, the proposed method can be used to prepare flexible fibrous composites characterized by a high surface area, flexibility, and light weight. These can be used for heterogeneous photocatalytic applications in water treatment, without the need of post treatment steps for their removal from the treated water which may restrict their wide applicability and cause secondary pollution.

Keywords: nanocomposite fibers; photocatalysis; mineralization; water remediation; organic pollutants

1. Introduction

The growing demand for clean water urges an improvement in commonly used methods for the wastewater management [1]. Depending on the type of water contamination, these conventional wastewater treatments can be physical, chemical, and biological processes [2]. However, these treatments present several limitations from a technological point of view, including the necessity for wastewater pre-treatment steps, secondary pollution, limited practicability, and often, low performance when emerging organic pollutants are involved [2–4]. For the removal of emerging and recalcitrant pollutants, new strategies have been proposed in combination with the available treatments. Among them, advanced oxidation processes (AOPs) can be used to ideally destroy organic pollutants from the contaminated water, thanks to the in situ production of strong oxidant species as the result of the interaction of the developed materials with solar, chemical, or other forms of energy [5–8].

Heterogeneous photocatalytic oxidation is one of the most promising AOPs for oxidizing organic pollutants into more biodegradable and less harmful compounds [5]. Typically, wide band gap, nano-

or micro-scale sized semiconductors are used as photocatalysts able to absorb incident photons causing the subsequent formation of a separation charge with a conduction-band electron and a valence-band hole. The photo-excited carriers can generate hydroxyl radicals and other reactive oxygen species (ROS), which react with the organic molecules present in the contaminated water causing their degradation, assuring an eco-compatible process since the oxidation occurs in mild conditions [5].

The semiconductor particles are usually dispersed in the contaminated water to ensure a high exposed surface area in contact with the pollutants, and therefore, a high volumetric generation rate of ROS. However, the main limitation in their use for water remediation applications is the demand of energy and time consuming additional steps for their recovery from the treated water. To avoid these post-treatment steps, the photo-catalyst powders can be immobilized on suitable solid supports [9,10]. To this aim, polymeric supports have been recently introduced due to their low weight, flexibility, and easy conversion in different morphologies [11–16]. Among them, fibrous polymeric mats have high surface area, which allows an enhanced interaction with the polluted water, and their preparation process is relatively simple and easily scaled up [9,17].

For the fabrication of the functional semiconductor based polymeric materials, an innovative approach has been recently proposed, dealing with the direct synthesis of NPs inside different polymeric matrices through a solid-state thermally, chemically, or photo-induced reaction [13,17–19]. Compared to traditional mixing processes, this approach offers the advantageous formation of NPs homogeneously distributed not only in the whole volume of the polymer matrix, but also exposed on its surface. Furthermore, limitations such as the complex rheology of polymer/NP solutions, which can limit their electrospin-ability and therefore the formation of fibrous nanocomposites, can be avoided [13,17]. Among the diverse types of nanocomposites developed so far following this approach [13,17,20], the ZnO-based mats is a promising system for the water remediation through the photocatalytic approach. In fact, ZnO is of great interest not only because it is environmental friendly, non-toxic, of low-cost, and abundant, but also because of its optoelectronic properties [9,21–24]. In particular, the n-type ZnO is a direct wide band gap semiconductor (band gap energy, $E_g = 3.37$ eV), characterized by a high exciton binding energy (60 meV), which allows efficient excitonic emission even at room temperature [25]. However, due to the high photo-generated electron–hole pair recombination, the photocatalytic performance and, therefore, the utilization of the ZnO in wastewater purification, can be limited. For this reason, the enhancement of the separated electron–hole lifetime is one of the factors on which the efforts are focused in order to improve the ZnO photocatalytic performance [26–28]. This aspect can be achieved through various methods, such as the modification of the morphology of the ZnO nanostructures [22,29], the incorporation of metallic [30,31] and non-metallic dopants [32] in their crystalline structure, and the preparation of hybridized structures with other materials [21,22,33,34].

Concerning the last method, the combination of ZnO NPs with noble metal NPs has been recently considered an effective route to enhance the local density of states at the metal–semiconductor interface, prolonging thus the electron–hole separation lifetime [21,33]. Specifically, the use of Au NPs to modify the ZnO surface has been proven to improve the photocatalytic performance of the semiconductor due to the surface plasmonic resonance effect (which allows the establishment of the Schottky barrier simplifying the charge carrier separation), the absorption in the visible range of the electromagnetic spectrum, and the ROS generation [35,36].

Considering the above, the development of Au/ZnO-based PMMA fibrous mats is here presented and their application in the remediation of organic aqueous pollutants through the heterogeneous photocatalytic approach is thoroughly explored. Specifically, ZnO NPs are synthesized by a thermally-induced solid state reaction directly in the electrospun polymeric fibers, obtaining an easily handleable flexible solid porous material. The subsequent dipping of the PMMA/ZnO composite mats in Au precursor solutions of different concentrations and their thermal treatment result in the direct formation of Au NPs on the surface of the fibers and, therefore, on the exposed ZnO NPs, forming a high metal–semiconductor interfacial area. Different concentrations of the Au precursor solutions are used to explore the effect of the amount, size, and localization of the formed Au NPs on the

ZnO/PMMA fiber surface. Moreover, the photocatalytic performance of the different nanocomposite mats under UV light irradiation is investigated, focusing on the degradation of the model molecule MB and of the emerging pollutant BPA. In particular, it is demonstrated that the presence of Au NPs affects significantly the photocatalytic performance of the PMMA/ZnO mat for both the organic pollutants. Therefore, with the presented straightforward fabrication method, it is possible to form light-weight and flexible polymeric fiber mats of high surface area that contain functional NP combinations for advanced photocatalytic applications. This valuable alternative to the existing systems paves the way to an innovative route for the fabrication of multifunctional membranes for water purification without the need of costly and time consuming post treatment separation processes as in the case of powders.

2. Materials and Methods

2.1. Materials

PMMA (average Mw ~350 kDa), zinc acetate dihydrate ($\text{Zn}(\text{CH}_3\text{CO}_2)_2$, 99,999%), *N,N*-dimethylformamide (DMF, $\geq 99.8\%$), chloroauric acid trihydrate ($\text{HAuCl}_4 \cdot 3\text{H}_2\text{O}$, 99.999%), MB, BPA ($\geq 99\%$), acetone ($\geq 99.5\%$), ethanol (EtOH, $\geq 99.8\%$), sodium hydroxide (NaOH, $\geq 98\%$, anhydrous), hydrochloric acid (HCl, 37%), and nitric acid (HNO_3 , 70%), were purchased from Sigma Aldrich, Italy. All chemicals were used without any further purification.

2.2. Preparation of PMMA/ZnO Composite Mats

The nanocomposite fibers were prepared as described elsewhere [17]. In brief, 1.5 g of PMMA were added in 10 mL of DMF and left under stirring at 50 °C until the complete dissolution; then 1.1 g (c.a. 40 wt %) of $\text{Zn}(\text{CH}_3\text{CO}_2)_2$ were added to the polymer solution and stirred at 40 °C, until a clear solution is obtained. The electrospinning technique was then used in a vertical setup to obtain the PMMA/ $\text{Zn}(\text{CH}_3\text{CO}_2)_2$ composite mats. The prepared solution was placed in a 10-mL syringe with a 22 G needle and the flow rate was set to $600 \mu\text{L} \cdot \text{h}^{-1}$. The voltage applied to the syringe needle was 23 kV and the grounded collector was kept at a distance of 16 cm from the needle. The electrospun fibers were then dried to remove the eventual residual solvent for 8 h under dynamic vacuum. The in situ growth of the ZnO NPs on the electrospun mats was achieved by placing the electrospun composite mats in a convection oven for 48 h at 110 °C, through the thermal decomposition of $\text{Zn}(\text{CH}_3\text{CO}_2)_2$.

The obtained PMMA/ZnO composite mats were then washed in 10 mL of a $\text{H}_2\text{O}/\text{EtOH}$ mixture (8:2 *v/v*) for 24 h and dried at 60 °C for 4 h. Following the methodology described to Section 2.4, it is defined that the total zinc loss during this washing step was around 1.170 ± 0.160 wt % of the total zinc. This can be attributed either to the loss of ZnO NPs not perfectly fixed on the surface of the fibers, or, also, to the water-soluble zinc acetate, which was not fully converted during the synthesis.

2.3. Preparation of PMMA/ZnO-Au Composite Mats

Three PMMA/ZnO composite mats (40 mg each) were dipped in 20 mL of a $\text{H}_2\text{O}/\text{EtOH}$ mixture (8:2 *v/v*) of $\text{HAuCl}_4 \cdot 3\text{H}_2\text{O}$, which was previously neutralized to pH 6.5 by NaOH_{aq} 0.1 M for 24 h in dark under gentle stirring. The aqueous-based $\text{HAuCl}_4 \cdot 3\text{H}_2\text{O}$ solution was prepared at different initial concentrations of gold precursor—1.5 mM, 3 mM, and 4.6 mM—to explore the effect of the different amounts of Au on the photocatalytic performance of the PMMA/ZnO-Au mats. The composite mats were then collected and washed three times with water. The reduction of the gold ions was obtained by the subsequent thermal treatment of the mats at 60 °C for 4 h, obtaining three PMMA/ZnO-Au samples named PMMA/ZnO-Au1, PMMA/ZnO-Au3, and PMMA/ZnO-Au6, respectively. Each sample was then divided in four similar pieces of 10 mg each for further analysis.

2.4. Characterization

The fiber morphology was investigated by a scanning electron microscope (SEM, JEOL JSM 6490LA, Tokyo, Japan) and a high-resolution scanning electron microscope (HR-SEM, JEOL JSM

7500FA, Tokyo, Japan), equipped with a cold field emission gun applying an accelerating voltage of 15 kV. The specimens were previously coated with a 10-nm-thick carbon layer by a carbon coater (Emitech K950X, Quorum Technologies Ltd., East Sussex, UK). The morphology of the ZnO and Au NPs in the composite mats was investigated by a transmission electron microscope (TEM, JEOL JEM 1400 Plus, Tokyo, Japan) operating at an acceleration voltage of 120 kV. To do so, the polymeric fibers were dissolved in acetone and the suspension was sonicated and centrifuged in order to separate the NPs from the polymer. Then, 30 μL of the suspension were deposited on a copper grid (CF300-Cu-UL, Electron Microscopy Science, USA) for further investigation. High-angle annular dark field scanning TEM (HAADF-STEM) images and energy dispersive X-ray spectroscopy (EDS) maps were acquired with a high-resolution FEI Tecnai G2 F20 (Oregon, USA) equipped with a Schottky field emission gun (FEG). The average size and the size distribution of the fibers and NPs were explored using the open source Fiji/ImageJ software.

The X-ray diffraction (XRD) analysis was performed on a PANalytical Empyrean X-ray diffractometer with a 1.8 kW $\text{CuK}\alpha$ ceramic X-ray tube ($\lambda = 1.5418 \text{ \AA}$) and a PIXcel^{3D} area detector ($2 \times 2 \text{ mm}^2$), operating at 45 kV and 40 mA. The diffractograms were recorded in parallel-beam geometry and symmetric reflection mode, for a 2θ range from 25° to 80° , with a step time of 383.67 s, and a step size of 0.026° . The average crystallite size was calculated by using the Debye–Scherrer equation (details in Supplementary Materials). The zinc and the gold content in the composite mats was obtained by ICP-OES analysis (iCAP 6300, Thermo, USA) of the digested solid samples. Specifically, 2.5 mL of aqua regia (HCl/HNO_3 , 3:1) were added to 2.5 mg of the composite fibers and the solid degradation reaction was performed by using a microwave digestion system (MARS Xpress, CEM) at 180°C for 15 min. The samples were then diluted with milliQ water up to 50 mL and filtered through polytetrafluoroethylene (PTFE) syringe filters (diameter 15 mm, pore size $0.45 \mu\text{m}$, Sartorius). In addition, to evaluate the loss of ZnO and Au NPs from the composite mats, the ICP-OES analysis was performed on the liquids after the photocatalytic degradation process. The samples (125 μL) were previously treated with 2.5 mL of aqua regia, and then they were diluted up to 25 mL with milliQ water and filtered through PTFE syringe filters (diameter 15 mm, pore size $0.45 \mu\text{m}$, Sartorius, Germany).

The optical properties of the nanocomposite fibers were evaluated by diffuse-reflectance measurements in the range between 200 and 800 nm, using a Varian Cary 6000i (Agilent, USA) UV-visible-NIR spectrophotometer equipped with integrating sphere. The energy bandgap (E_g) of ZnO and ZnO/Au NPs was then extrapolated by applying the Kubelka-Munk method to the reflectance results (see Supplementary Materials). The Raman spectra of the composite mats were acquired by a Raman LabRam HR800 (Horiba Jobin-Yvon Inc., France) spectrometer equipped with a built-in microscope with objectives $10\times$ (NA 0.25) and $50\times$ (NA 0.75), using the 632.8 nm He-Ne laser excitation. The experimental setup consists of a grating $600 \text{ lines}\cdot\text{mm}^{-1}$ with a spectral resolution of approximately 1 cm^{-1} .

2.5. Photocatalytic Performance

The photocatalytic performance of the developed materials was evaluated by immersing 10 mg of the mats in quartz cuvettes filled with 3 mL of MB or BPA aqueous solutions (0.0125 mM and 0.044 mM, respectively). To evaluate the adsorption of the organic molecules on the developed mats, experiments in dark conditions were performed overnight. For the photocatalytic experiments, the solutions containing the samples were placed at a distance of 10 cm under a UVA lamp emitting at a wavelength range from 315 nm to 400 nm ($937 \mu\text{W}/\text{cm}^2$ at 365 nm, 10 cm from source) connected to a climatic chamber (ICH 110 L, Memmert, Germany). The UVA irradiance ($\mu\text{W}/\text{cm}^2$) of the UV light source was measured by using a combined photo-radiometric probe (LP 471 P-A, Delta Ohm, Italy) at the fixed experimental distances between the source and the samples. Before starting the UV irradiation, the mats were maintained in the dark for 60 min. The decrease of the organic molecule concentrations was monitored by recording the UV-vis absorption spectra at specific time intervals.

The test was also performed for a reference sample, namely a quartz cuvette filled with the MB or BPA solution, in order to estimate the self-degradation of the pollutants under the UV light irradiation.

The photocatalytic degradation efficiency ($DE\%$) was obtained from the Equation (1), while the first-order rate constant (k_1, min^{-1}) was calculated by fitting the experimental data of the first 5 h of irradiation with the pseudo-first order model expressed in Equation (2)

$$DE\% = \left(1 - \frac{C}{C_0}\right) \cdot 100 \quad (1)$$

$$\ln\left(\frac{C_0}{C}\right) = k_1 t \quad (2)$$

in which C_0 is the initial pollutant concentration and C is the concentration at t irradiation time. The organic molecule concentrations were determined by using two calibration curves with linear regression (R^2 values of 0.9983 and 0.9998 for MB and BPA, respectively). For the MB, the calibration curve was obtained by monitoring the absorbance of the MB at the wavelength of maximum absorbance ($\lambda_{\text{max}} = 664 \text{ nm}$) with concentrations ranging from 0.00087 to 0.0125 mM. For the BPA calibration curve, the aqueous solution concentrations ranged from 0.0031 to 0.05 mM, and the absorbance variation was monitored at 276 nm.

Before and after the photocatalytic degradation of the organic molecules, the total organic carbon (TOC) of the solutions was analyzed by a membraPure uniTOC lab analyzer, Gemany. The total amount of organic bound carbon in the aqueous samples was measured by mean of a UV/reagent promoted oxidation into carbon dioxide (CO_2) which was then quantified by the non-dispersive infrared detector. After the photocatalytic degradation experiment, the MB and BPA aqueous solutions were collected from the quartz cuvettes and diluted with MilliQ water, in order to reach 15 mL in each case. To remove any possible solid residue, the aqueous solutions were centrifuged and then filtered using a polytetrafluoroethylene (PTFE) syringe filters (diameter 15 mm, pore size 0.20 μm , Sartorius, Germany). The reagent used was an acidic aqueous solution of sodium persulfate (10% $_{\text{W/V}}$) and phosphoric acid (3% $_{\text{V/V}}$). The inorganic carbon content was firstly removed and measured by the internal acidification step. The TOC value was used to evaluate the mineralization of the MB and of the BPA, and therefore, the efficiency of the photocatalytic degradation.

The stability of the composite mats was evaluated by repeating the photocatalytic experiments on the same samples over three cycles. The composite mats were washed before starting the subsequent cycle by dipping in clean water for 1 h under UV light irradiation (same conditions as previously described) in order to remove the possible adsorbed pollutants.

3. Results

The electrospun composite mats (photographs shown in Figure S1 in the Supplementary Materials) consisted of continuous defect-free polymeric fibers characterized by smooth surface, whose random distribution resulted in the formation of a porous material. Compared to the PMMA fibers (Figure S2), the PMMA/ $\text{Zn}(\text{CH}_3\text{CO}_2)_2$ fibers exhibited a higher mean diameter with a broader size distribution, while their morphology remained rather similar, in accordance with our previous work [17]. In particular, even if the electrospinning operating parameters were preserved, the mean diameter of the polymeric fibers increased from 1.5 ± 0.3 to $6.2 \pm 3.7 \mu\text{m}$ (for PMMA and PMMA/ $\text{Zn}(\text{CH}_3\text{CO}_2)_2$, respectively). This difference was mainly due to the presence of the high content of $\text{Zn}(\text{CH}_3\text{CO}_2)_2$ which causes the enhancement of the viscosity of the solution (from $1.57 \pm 0.05 \text{ Pa}\cdot\text{s}$ to $4.10 \pm 0.15 \text{ Pa}\cdot\text{s}$) [17].

After the thermal treatment of the PMMA/ $\text{Zn}(\text{CH}_3\text{CO}_2)_2$ fibrous mats, ZnO NPs were formed, well distributed on the surface of the fibers but also in their bulk, as shown in Figure 1a and Figure S3. The content of ZnO NPs obtained after the zinc salt conversion was about $11.7 \pm 0.9 \text{ wt.}\%$ with respect to the composite, as calculated by the ICP-OES analysis. Apart the ZnO NPs formation, it should be mentioned that the thermal treatment did not affect the overall size distribution of the polymeric fibers,

which remained unchanged (Figure S3b). In order to obtain the ZnO/Au NPs hybrid structures on the polymeric fibers, the PMMA/ZnO composite mats were dipped in the gold precursor aqueous solutions of different initial concentrations. The neutralization of the acidic gold precursor solution, performed to avoid the solubilization of the amphoteric ZnO NPs, determined the presence of $[\text{AuCl}_2(\text{OH})_2]^-$ species which were favorably adsorbed on the positively charged surface of the ZnO NPs.

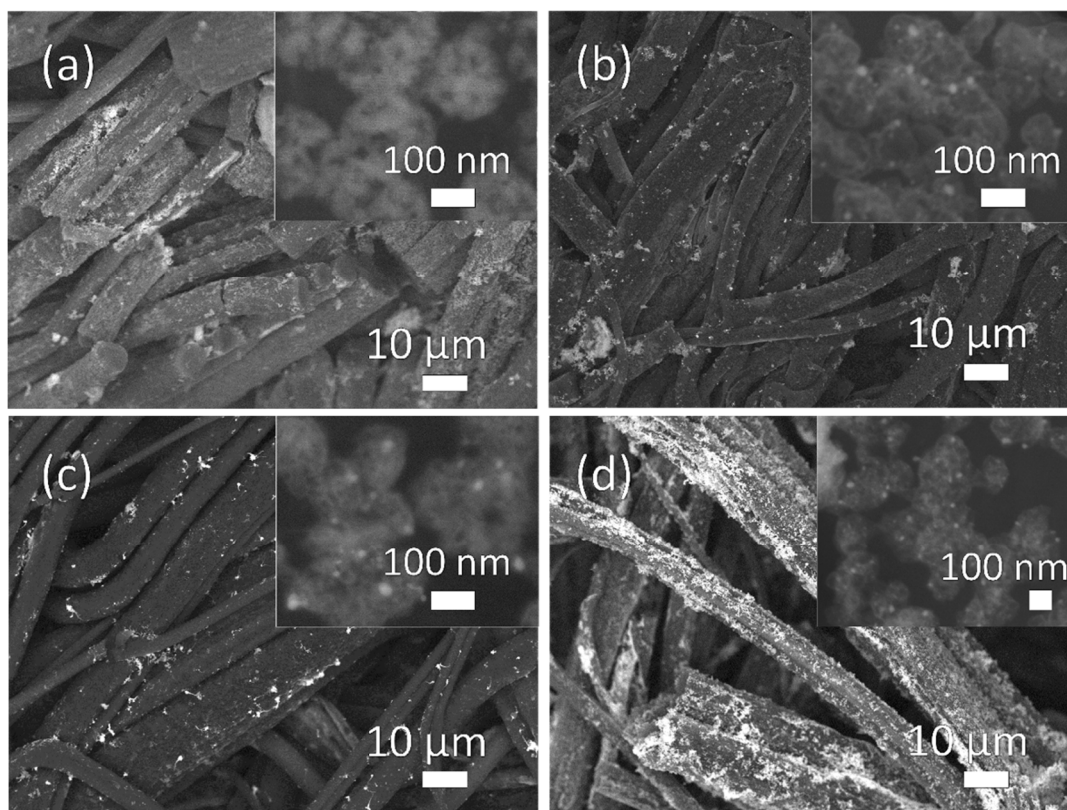


Figure 1. High-resolution scanning electron microscope (HRSEM) images of the (a) PMMA/ZnO, (b) PMMA/ZnO-Au1, (c) PMMA/ZnO-Au3, and (d) PMMA/ZnO-Au6 composite mats. Insets report the details on the surface of the different composite mats. PMMA: poly(methyl methacrylate).

The subsequent thermal treatment led to the formation of Au NPs on the surface of the fibers, which appeared not to be further affected by these steps. In fact, as shown in Figure 1b–d, the formed Au NPs appeared well distributed on the surface of the composite mats. The Au NPs were mainly attached on the surface of the ZnO NPs, as shown in the corresponding insets of the Figure 1b–d, while their size was not significantly affected by the initial concentration of the gold precursor solution. However, a higher initial concentration of the gold precursor solution led to an increase in the coverage of the composite fibers by the Au NPs, which, for the highest concentration (PMMA/ZnO-Au6), tended to form nanowires and aggregate on the surface of the composite mats. The amount of Au NPs formed on the composite mats was approximately 1%, 3%, and 6% wt. of Au with respect to the composite, for PMMA/ZnO-Au1, PMMA/ZnO-Au3, and PMMA/ZnO-Au6 respectively, as defined from the ICP-OES analysis.

As shown in Figure 2a,b, the formed ZnO NPs had a spherical branched structure with an average diameter of 135 ± 38 nm, which, in accordance with the SEM analysis, corresponded to the NPs grown on the surface of the fibers (Figure S3a). The selected area electron diffraction (SAED) pattern, inset of Figure 2a, confirmed the attribution of the NPs to ZnO of hexagonal wurtzite phase. In Figure S4a it is possible to observe also the presence of smaller irregular ZnO NPs. This second type of particles was formed in the internal part of the polymeric fibers (inset of Figure S3a), which restrained their growth [17].

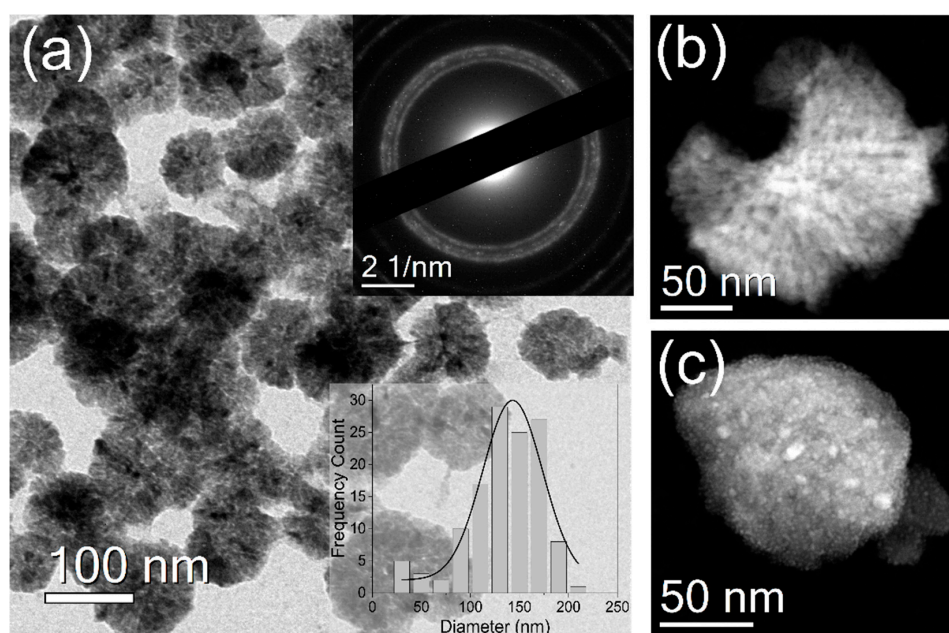


Figure 2. (a) Transmission electron microscope (TEM) image of the ZnO nanoparticles (NPs). The two insets show the selected area electron diffraction (SAED) pattern and the diameter size distribution of the NPs. Dark-field TEM images of (b) ZnO and of (c) ZnO decorated with Au NPs.

After the dipping in the gold precursor solutions of the PMMA/ZnO fibers and the subsequent heating process, small Au NPs were grown, mainly localized on the surface of the ZnO NPs, as shown in Figure 2c and in the EDS maps of Figure S5. In all the composite mats, the formed Au NPs had an average diameter of c.a. 8 ± 3 nm, 13 times smaller than the ZnO branched NPs. The lower mean diameter of the Au NPs compared to the ZnO allowed a high superficial contact between the two types of NPs and, therefore, an efficient charge separation.

The structures and the crystallites size of the ZnO NPs in the different composite mats were explored by XRD analysis (Figure 3). In all the composite mats, the ZnO NPs exhibited the characteristic diffraction peaks of the hexagonal wurtzite phase. In presence of Au NPs, a new diffraction peak appeared at 38° , which was assigned to the (111) crystal plane of the cubic Au phase. For the PMMA/ZnO-Au6 composite mat, it was also possible to observe an additional diffraction peak at 44° , related to the Au (002) lattice plane due to the higher amount of Au NPs on the surface compared to the other composite mats. The presence of Au did not cause shifts of the position of the ZnO diffraction peaks, and therefore the crystal structure of the ZnO NPs was not affected by the post-synthetic growth of the Au NPs. Furthermore, no extra phase or other peaks were observed, confirming the absence of crystalline impurities inside the samples. The average crystallite size of the ZnO NPs was approximated to 9 nm, as estimated by using the Debye–Scherrer equation.

The metal–semiconductor interface in the Au/ZnO NPs hybrid structure was investigated through diffuse reflectance and Raman spectroscopy. The diffuse reflectance spectra of the different composite mats are shown in Figure 4a. In all cases, it is possible to observe the characteristic absorption of the ZnO NPs in the UV region originated by the direct band gap transitions [26]. The presence of the Au NPs led to the addition of another absorption band with a maximum at 550 nm, attributed to the surface plasmon resonance of the Au NPs. The E_g of the ZnO was estimated by applying the Kubelka–Munk (KM) method to the data obtained by the reflectance spectra (details of the KM equation and graphical representation can be found in Supplementary Materials and Figure S6). The calculated E_g values demonstrate that the presence of the Au NPs did not cause any modification to the E_g of the ZnO present in the composite mats. In particular, the E_g was 3.25 ± 0.01 eV for the PMMA/ZnO, and 3.23 ± 0.02 eV, 3.23 ± 0.04 eV, and 3.25 ± 0.01 eV for the PMMA/ZnO-Au1, PMMA/ZnO-Au3, and PMMA/ZnO-Au6, respectively.

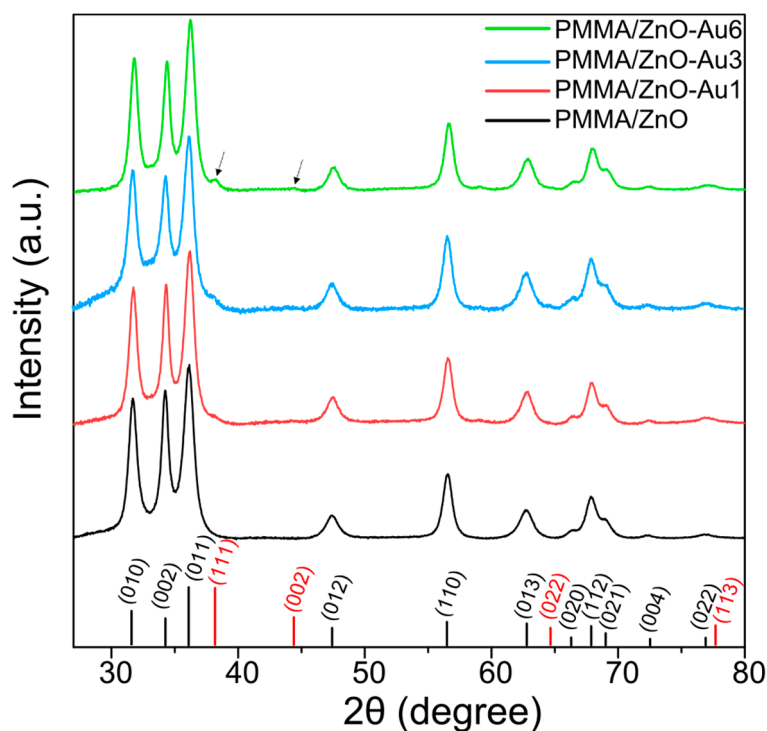


Figure 3. X-ray diffraction (XRD) patterns of the different composite mats. Stick reference pattern of ZnO (black) and of Au (red) are shown along the x-axis. The arrows indicate the detected Au diffraction peaks.

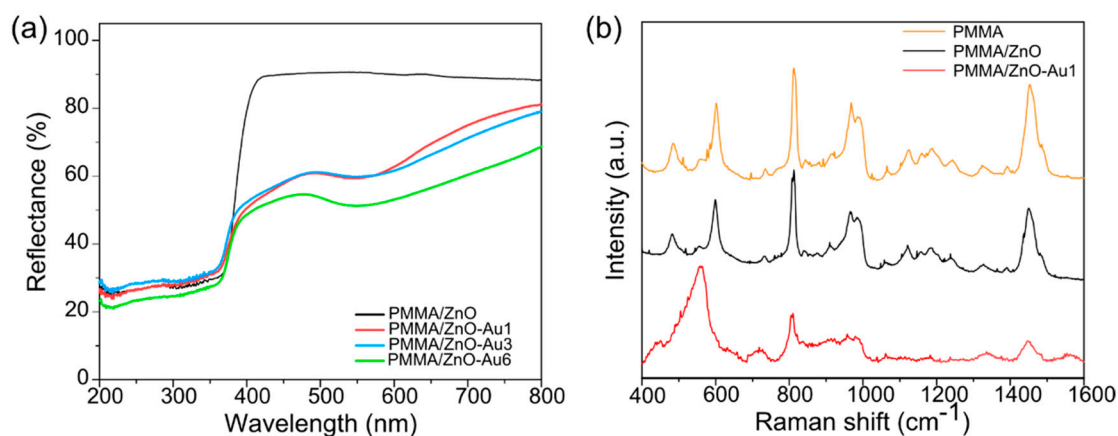


Figure 4. (a) Diffusive reflectance spectra of the developed composite mats. (b) Raman spectra of the polymeric fibers and of the PMMA/ZnO before and after the superficial modification with Au NPs.

The formation of the Au/ZnO NP hybrid structures was confirmed by Raman spectroscopy. Typically, the optical phonon modes predicted by the group theory for the hexagonal wurtzite ZnO structures are the polar Raman and infrared active modes A_1 , E_1 , the non-polar Raman active $2E_2$, and the silent $2B_1$ modes. The A_1 and E_1 modes are split in the transverse optical (TO) and longitudinal optical (LO) modes with different frequencies due to the manifestation of the macroscopic electric field of the LO phonons. The two E_2 are split in the high- and low-frequency modes (E_2^{high} and E_2^{low}) which are associated with the oxygen atoms and the zinc sublattice, respectively [37,38]. In the Raman spectrum of the PMMA/ZnO composite mat (Figure 4b), all the peaks observed were attributed to the PMMA [39], whose assignments are listed in Supplementary Materials (Table S1), while the Raman active modes of the wurtzite ZnO were not evident, possibly due to the presence of the polymer matrix

and to the used experimental conditions [40]. It was possible to observe the characteristic modes of the ZnO only after the plasmonic enhancement provided by the contact with the Au NPs in the ZnO/Au hybrid systems. In fact, in the Raman spectrum of PMMA/ZnO-Au1 (Figure 4b), additional peaks appeared at 450 cm^{-1} and 560 cm^{-1} , which were respectively assigned to the E_2^{high} and $A_1(\text{LO})$ modes of the ZnO, proving the non-resonant surface enhanced Raman scattering of the ZnO optical modes in the proximity of Au NPs [37,41,42]. The Raman spectra of the PMMA/ZnO-Au3 and PMMA/ZnO-Au6 (Figure S7) show analogue enhancement of the Raman scattering of the ZnO optical modes.

The effect of different amounts of Au NPs on the photocatalytic degradation performance of the composite mats was then investigated using MB and BPA aqueous solutions. The MB is a cationic dye which can be found in wastewater deriving mainly from the textile, paper, and plastic industries. It is commonly adopted as a model pollutant for testing the photocatalytic performance of various materials under UV light irradiation. BPA is a recalcitrant aqueous pollutant classified as an endocrine disruptor, and is widely present in water due to its broad applications in the plastic industry [43]. In order to evaluate the adsorption of the organic pollutants on the fibrous composites, the mats were dipped in the organic pollutant solutions in dark conditions. As shown in Figure S8, there was a negligible MB adsorption on the fibers. The concentration of BPA slightly decreased over time in the presence of the PMMA/ZnO and of the PMMA/ZnO-Au with 1 wt % and 3 wt % Au contents. On the contrary, the PMMA/ZnO-Au6 showed a higher adsorption capacity compared to the other composites, adsorbing c.a. 39% of the initial BPA, due to the instauration of dispersive bonding interactions between the aromatic rings of the BPA and the gold surface, which was in a relatively high amount on the composite fibers [44,45].

Under UV irradiation (Figure 5), the concentration of both organic pollutants decreased in time only in the presence of the nanocomposite fibrous mats. In fact, their self-degradation was negligible, while for the pure PMMA fibrous mat there was no significant change in the concentration of the pollutants, confirming the absence of photocatalytic activity. When the composite mats were dipped in the solutions, it was possible to observe a more efficient photocatalytic degradation of the organic pollutants in the presence of the Au/ZnO hybrid structures.

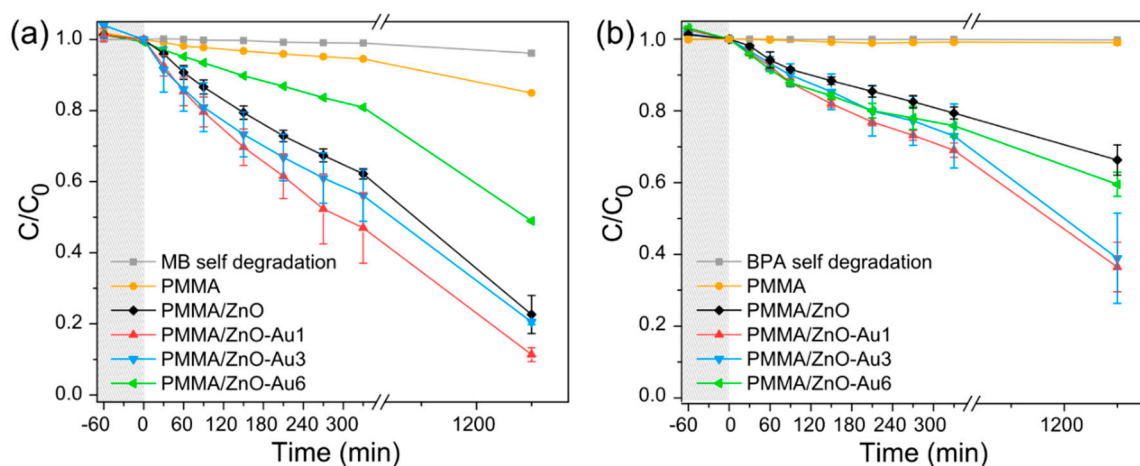


Figure 5. Photocatalytic degradation curves of (a) methylene blue (MB) and (b) bisphenol A (BPA) in presence of the composite mats under UV light. Before the UV irradiation, the solutions were kept in dark for 60 min in the presence of the composite mats. The self-degradation of MB and BPA under UV is also presented.

As shown in Figure 5a, the PMMA/ZnO mat was able to decolorize 77% of the initial MB solution while in the presence of the PMMA/ZnO-Au1, the efficiency reached 88% after 20 h of irradiation. By increasing the content of Au, the MB photocatalytic degradation tended to slightly decrease, reaching 80% for the PMMA/ZnO-Au3, while for the PMMA/ZnO-Au6, it was lower compared to that

observed for the PMMA/ZnO (Figure 5a). The photocatalytic degradation curves of the pollutants followed a pseudo-first order kinetic model for all the developed composite mats (Figure S9), and the enhanced performance of the PMMA/ZnO-Au1 composite was also reflected on its k_1 for the first 5 h of irradiation. In fact, the photocatalytic degradation of MB with the PMMA/ZnO-Au1 reached the maximum value of k_1 $2.33 \times 10^{-3} \text{ min}^{-1}$, significantly higher than that obtained using the PMMA/ZnO, $1.44 \times 10^{-3} \text{ min}^{-1}$ and the other composite mats, as shown in Table S3 in the Supplementary Materials.

A similar behavior is also observed for the photocatalytic degradation of BPA. As shown in Figure 5b, the PMMA/ZnO-Au1 induced a 63.5% decrease of the initial BPA concentration after 20 h of UV irradiation, remarkably higher compared to the BPA reduction achieved with the PMMA/ZnO mat ($DE\%$ of 34%). For higher amounts of Au NPs, the photocatalytic degradation efficiency was around 61% and 41%, for the PMMA/ZnO-Au3 and PMMA/ZnO-Au6, respectively. The k_1 values calculated by applying the first order kinetics model on the experimental data were in accordance with the photodegradation efficiency results. The PMMA/ZnO-Au1 displayed a faster reaction rate ($1.12 \times 10^{-3} \text{ min}^{-1}$) compared to the PMMA/ZnO-Au3 and PMMA/ZnO-Au6 (0.96×10^{-3} and $0.82 \times 10^{-3} \text{ min}^{-1}$ respectively) and to the PMMA/ZnO (k_1 $0.69 \times 10^{-3} \text{ min}^{-1}$). Despite the results obtained for the MB, the PMMA/ZnO-Au6 composite mat displayed a more effective reduction of the initial BPA concentration compared to the PMMA/ZnO mat. However, this is not attributed to the photocatalytic degradation but to the high adsorption of the BPA on the surface of the Au NPs, as demonstrated with the adsorption experiment (Figure S8b).

For both the pollutants studied, the enhanced photocatalytic activity using the PMMA/ZnO-Au1 hybrid structures indicates that the specific ZnO-Au combination is favorable for the formation of the Schottky barrier at the metal–semiconductor interface, which enhances the charge carrier separation and therefore the ROS formation [21,46]. In fact, as observed in the SEM analysis, when the content of Au was low, the NPs were better distributed on the fibers without forming large aggregates, as in the case of higher amount of Au (PMMA/ZnO-Au6). The presence of Au aggregates on the ZnO NPs catalyst causes a decrease of their active surface exposed towards the organic pollutants and also a less effective light penetration due to a screening effect [22,28,47]. This result is also confirmed by previous studies; as a matter of fact, there is an optimal concentration of metallic NPs for the surface modification of the metal oxide semiconductors, beyond which the photocatalytic performance declines [46,48].

In order to evaluate the conversion of the organic pollutants into CO_2 and, therefore, the efficiency of the developed materials to mineralize the organic pollutants upon photocatalytic degradation, the mineralization of MB and BPA has been investigated by TOC studies of the solutions before and after the irradiation experiments. Based on the obtained results (Table S2 in Supplementary Materials), it can be assured that 60% of MB is mineralized in the presence of the PMMA/ZnO-Au1 mat upon UV irradiation, higher compared to the 45.5% obtained using the PMMA/ZnO. In the case of BPA, the PMMA/ZnO-Au1 was able to mineralize the 15% of the 63.5% photodegraded molecules, while no changes in the TOC were detected after using PMMA/ZnO. The lower mineralization of BPA compared to that obtained for MB can be ascribed to the recalcitrant nature of this organic pollutant. The effective removal of the BPA molecules is greatly challenging due to their complex aromatic structure, which, together with their low biodegradability, makes BPA one of the principal pollutants detected in the effluents of the wastewater treatment plants [49].

Since the PMMA/ZnO-Au1 mats show the best performance in terms of photocatalytic degradation of both MB and BPA organic pollutants, their stability is investigated by performing three consecutive irradiation cycles. The loss of Zn and Au from the composite mats was negligible after the first irradiation cycle, since about $0.022 \pm 0.001 \text{ wt } \%$ of Zn with respect to the total Zn amount in the composites was detected in the liquids, while the content of Au was well below the instrument's detection limit. The overall photocatalytic performance of the PMMA/ZnO-Au1 was maintained unvaried for two consecutive cycles in terms of degradation efficiency of MB (Figure 6a), while, in the third cycle, the performance slightly decreased to 72.5%. This was also the case of the PMMA/ZnO sample (Figure S10a of Supplementary Materials) indicating the fact that this reduction in

the performance can be possibly attributed to a low photo-corrosion effect of the ZnO [50]. In the case of BPA, the photocatalytic performance of the PMMA/ZnO-Au1 showed a more evident decrease after the second cycle compared to that observed for the MB, lowering further in the third cycle (Figure 6b). Despite this reduction, the degradation efficiency of the third cycle was higher than that reached for the PMMA/ZnO mat, in which only 10% of the BPA was photodegraded (Figure S10b). This aspect confirms the improvement of the catalytic activity of the mat due to the presence of 1% of Au NPs also in the removal of a recalcitrant aqueous pollutant.

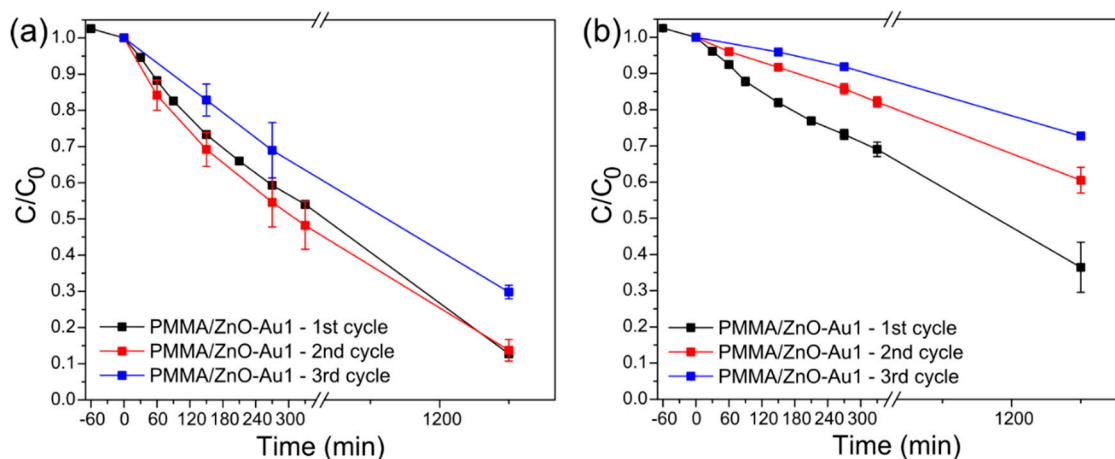


Figure 6. Photocatalytic degradation activity under UV light irradiation of (a) MB and (b) BPA for three consecutive cycles using the PMMA/ZnO-Au1.

4. Conclusions

The enhancement of the photocatalytic activity of the PMMA/ZnO composite mats was here investigated through a surface modification of the semiconductor nanostructures with Au NPs by means of a straightforward fabrication approach. The hybrid Au/ZnO nanostructures were fixed on a polymeric support through a thermally induced solid-state synthesis and a subsequent adsorption dipping process. Thanks to this accessible and scalable fabrication procedure, the Au/ZnO nanostructures were formed directly on the surface of electrospun polymeric fibers, obtaining a flexible, easily handleable, and light-weight porous system. The photoactive material was stable on the polymeric matrix, since its loss in water after 24 h was negligible. The presence of 1% of Au NPs on the PMMA/ZnO composite mats enhanced the photocatalytic degradation and the mineralization of both the organic pollutants studied, MB and BPA. In fact, the Au NPs were homogeneously distributed on the surface of the ZnO NPs without the formation of aggregates, thus allowing an effective metal–semiconductor interface, which is fundamental for the improvement of the photocatalytic performance of the ZnO under UV light irradiation. Although the BPA degradation was less effective than that obtained for MB, due to the intrinsic nature of the BPA molecules, the presence of Au significantly improved the photodegradation performance of ZnO for such a persistent pollutant. Therefore, the proposed fabrication approach can be considered a valid alternative to the conventional routes for the development of efficient supported photocatalysts for water remediation applications.

Supplementary Materials: The following are available online at <http://www.mdpi.com/2073-4441/11/9/1787/s1>, Details on the Debye–Scherrer equation and Kubelka–Munk method, Figure S1: Photos of (a) PMMA/ZnO, (b) PMMA/ZnO-Au1, (c) PMMA/ZnO-Au3, and (d) PMMA/ZnO-Au6. Figure S2: SEM images and size distribution analysis of the diameter of the fibers of (a,b) PMMA and (c,d) PMMA/Zn(CH₃CO₂)₂ mats. Figure S3: (a) HRSEM image of PMMA/ZnO with cross-sectional detail. (b) Diameter size distribution of the PMMA/ZnO composite mat. Figure S4: TEM images of (a) the smaller ZnO NPs formed in the bulk of the polymeric fibers and of (b) the ZnO/Au hybrid structure in the PMMA/ZnO-Au1 composite mat. Figure S5: Dark field TEM image of (a) the ZnO-Au hybrid structure and EDS mapping of (b) Au, (c) Zn, and (d) O. Figure S6: Kubelka–Munk plots of the composite mats. The energy band gap is extrapolated from a linear regression. Table S1: Assignment of the Raman modes of the PMMA. Figure S7: Raman spectra of PMMA/ZnO-Au3 and PMMA/ZnO-Au6. Figure S8: Evolution

of the normalized concentration of (a) MB and (b) BPA solutions in presence of the developed mats in dark. Table S2: Degradation and mineralization values obtained from the photocatalytic degradation of the MB and BPA aqueous solution in presence of the mats after 20 h under UV light irradiation. Figure S9: The pseudo-first-order reaction kinetics for (a) MB and (b) BPA, applied on the experimental data obtained in the first 5 h of reaction. Table S3: Photo-degradation rate constants and linear regression coefficients obtained from the linear fitting of the experimental data by using the pseudo-first order model. Figure S10: Photocatalytic degradation activity of (a) MB and (b) BPA for three consecutive UV irradiation cycles using PMMA/ZnO composite mats.

Author Contributions: L.C. and D.F. conceived and designed the experiments. L.C. realized the materials, performed the characterizations and the photocatalytic experiments, analyzed the data, and accomplished the original draft. S.L. acquired HRSEM images and contributed to the draft editing. A.A. provided the funding and the resources. D.F. supervised the research, validated the results, and edited and reviewed the draft.

Funding: This research received no external funding.

Acknowledgments: The authors kindly acknowledge Alice Scarpellini for the acquisition of the dark-field TEM images and Filippo Drago for the ICP-OES analysis. The useful discussion with Davide Morselli concerning the preparation and the characterization of the materials is also gratefully acknowledged.

Conflicts of Interest: The authors declare no conflict of interest. The funders had no role in the design of the study; in the collection, analyses, or interpretation of data; in the writing of the manuscript, or in the decision to publish the results.

References

1. Hernández-Chover, V.; Bellver-Domingo, Á.; Hernández-Sancho, F. Efficiency of wastewater treatment facilities: The influence of scale economies. *J. Environ. Manage.* **2018**, *228*, 77–84. [[CrossRef](#)] [[PubMed](#)]
2. Crini, G.; Lichtfouse, E. Advantages and disadvantages of techniques used for wastewater treatment. *Environ. Chem. Lett.* **2019**, *17*, 145–155. [[CrossRef](#)]
3. Luo, J.; Zhang, Q.; Cao, J.; Fang, F.; Feng, Q. Importance of monitor and control on new-emerging pollutants in conventional wastewater treatment plants. *J. Geosci. Environ. Prot.* **2018**, *6*, 55–58. [[CrossRef](#)]
4. Matamoros, V.; Rodríguez, Y.; Albaigés, J. A comparative assessment of intensive and extensive wastewater treatment technologies for removing emerging contaminants in small communities. *Water Res.* **2016**, *88*, 777–785. [[CrossRef](#)] [[PubMed](#)]
5. Fiorenza, R.; Bellardita, M.; D'Urso, L.; Compagnini, G.; Palmisano, L.; Scirè, S. Au/TiO₂-CeO₂ catalysts for photocatalytic water splitting and VOCs oxidation reactions. *Catalysts* **2016**, *6*, 121. [[CrossRef](#)]
6. Miklos, D.B.; Remy, C.; Jekel, M.; Linden, K.G.; Drewes, J.E.; Hübner, U. Evaluation of advanced oxidation processes for water and wastewater treatment—A critical review. *Water Res.* **2018**, *139*, 118–131. [[CrossRef](#)] [[PubMed](#)]
7. Philippe, K.K.; Timmers, R.; Van Grieken, R.; Marugan, J. Photocatalytic disinfection and removal of emerging pollutants from effluents of biological wastewater treatments, using a newly developed large-scale solar simulator. *Ind. Eng. Chem. Res.* **2016**, *55*, 2952–2958. [[CrossRef](#)]
8. Amor, C.; Marchão, L.; Lucas, M.S.; Peres, J.A. Application of advanced oxidation processes for the treatment of recalcitrant agro-industrial wastewater: A review. *Water* **2019**, *11*, 205. [[CrossRef](#)]
9. Ognibene, G.; Cristaldi, D.A.; Fiorenza, R.; Blanco, I.; Cicala, G.; Scirè, S.; Fragalà, M.E. Photoactivity of hierarchically nanostructured ZnO-PES fibre mats for water treatments. *RSC Adv.* **2016**, *6*, 42778–42785. [[CrossRef](#)]
10. Maučec, D.; Šuligoj, A.; Ristić, A.; Dražić, G.; Pintar, A.; Tušar, N.N. Titania versus zinc oxide nanoparticles on mesoporous silica supports as photocatalysts for removal of dyes from wastewater at neutral pH. *Catal. Today* **2018**, *310*, 32–41. [[CrossRef](#)]
11. Neghi, N.; Kumar, M.; Burkhalov, D. Synthesis and application of stable, reusable TiO₂ polymeric composites for photocatalytic removal of metronidazole: Removal kinetics and density functional analysis. *Chem. Eng. J.* **2019**, *359*, 963–975. [[CrossRef](#)]
12. Podasca, V.E.; Buruiana, T.; Buruiana, E.C. Photocatalytic degradation of Rhodamine B dye by polymeric films containing ZnO, Ag nanoparticles and polypyrrole. *J. Photochem. Photobiol. A Chem.* **2019**, *371*, 188–195. [[CrossRef](#)]
13. Morselli, D.; Campagnolo, L.; Prato, M.; Papadopoulou, E.L.; Scarpellini, A.; Athanassiou, A.; Fragouli, D. Ceria/gold nanoparticles in situ synthesized on polymeric membranes with enhanced photocatalytic and radical scavenging activity. *ACS Appl. Nano Mater.* **2018**, *1*, 5601–5611. [[CrossRef](#)]

14. Colmenares, J.C.; Kuna, E. Photoactive hybrid catalysts based on natural and synthetic polymers: A comparative overview. *Molecules* **2017**, *22*, 790. [[CrossRef](#)] [[PubMed](#)]
15. Di Mauro, A.; Cantarella, M.; Nicotra, G.; Pellegrino, G.; Gulino, A.; Brundo, M.V.; Privitera, V.; Impellizzeri, G. Novel synthesis of ZnO/PMMA nanocomposites for photocatalytic applications. *Sci. Rep.* **2017**, *7*, 1–12. [[CrossRef](#)]
16. Hegedűs, P.; Szabó-Bárdos, E.; Horváth, O.; Szabó, P.; Horváth, K. Investigation of a TiO₂ photocatalyst immobilized with poly(vinyl alcohol). *Catal. Today* **2016**, *285*, 179–186. [[CrossRef](#)]
17. Morselli, D.; Valentini, P.; Perotto, G.; Scarpellini, A.; Pompa, P.P.; Athanassiou, A.; Fragouli, D. Thermally-induced in situ growth of ZnO nanoparticles in polymeric fibrous membranes. *Compos. Sci. Technol.* **2017**, *149*, 11–19. [[CrossRef](#)]
18. Pinto, J.; Morselli, D.; Bernardo, V.; Notario, B.; Fragouli, D.; Rodriguez-Perez, M.A.; Athanassiou, A. Nanoporous PMMA foams with templated pore size obtained by localized in situ synthesis of nanoparticles and CO₂ foaming. *Polymer* **2017**, *124*, 176–185. [[CrossRef](#)]
19. Feng, J.; Athanassiou, A.; Bonaccorso, F.; Fragouli, D. Enhanced electrical conductivity of poly(Methyl methacrylate) filled with graphene and in situ synthesized gold nanoparticles. *Nano Futur.* **2018**, *2*, 025003. [[CrossRef](#)]
20. Demir, M.M.; Gulgun, M.A.; Menciloglu, Y.Z.; Erman, B.; Abramchuk, S.S.; Makhaeva, E.E.; Khokhlov, A.R.; Matveeva, V.G.; Sulman, M.G. Palladium nanoparticles by electrospinning from Poly(acrylonitrile-co-acrylic acid)-PdCl₂ solutions. relations between preparation conditions, particle size, and catalytic activity. *Macromolecules* **2004**, *37*, 1787–1792. [[CrossRef](#)]
21. Andrade, G.R.S.; Nascimento, C.C.; Lima, Z.M.; Teixeira-Neto, E.; Costa, L.P.; Gimenez, I.F. Star-shaped ZnO/Ag hybrid nanostructures for enhanced photocatalysis and antibacterial activity. *Appl. Surf. Sci.* **2017**, *399*, 573–582. [[CrossRef](#)]
22. Thanh, Q.; Ta, H.; Park, S.; Noh, J. Ag nanowire/ZnO nanobush hybrid structures for improved photocatalytic activity. *J. Colloid Interface Sci.* **2017**, *505*, 437–444. [[CrossRef](#)] [[PubMed](#)]
23. He, X.; Yang, D.P.; Zhang, X.; Liu, M.; Kang, Z.; Lin, C.; Jia, N.; Luque, R. Waste eggshell membrane-templated CuO-ZnO nanocomposites with enhanced adsorption, catalysis and antibacterial properties for water purification. *Chem. Eng. J.* **2019**, *369*, 621–633. [[CrossRef](#)]
24. Ussia, M.; Di Mauro, A.; Mecca, T.; Cunsolo, F.; Nicotra, G.; Spinella, C.; Cerruti, P.; Impellizzeri, G.; Privitera, V.; Carroccio, S.C. ZnO-pHEMA nanocomposites: An Ecofriendly and Reusable Material for Water Remediation. *ACS Appl. Mater. Interfaces* **2018**, *10*, 40100–40110. [[CrossRef](#)] [[PubMed](#)]
25. Su, Y.Q.; Zhu, Y.; Yong, D.; Chen, M.; Su, L.; Chen, A.; Wu, Y.; Pan, B.; Tang, Z. Enhanced Exciton Binding Energy of ZnO by Long-Distance Perturbation of Doped Be Atoms. *J. Phys. Chem. Lett.* **2016**, *7*, 1484–1489. [[CrossRef](#)] [[PubMed](#)]
26. Guidelli, E.J.; Baffa, O.; Clarke, D.R. Enhanced UV Emission from Silver/ZnO and Gold/ZnO Core-Shell Nanoparticles: Photoluminescence, Radioluminescence, and Optically Stimulated Luminescence. *Sci. Rep.* **2015**, *5*, 1–11. [[CrossRef](#)]
27. Li, P.; Wei, Z.; Wu, T.; Peng, Q.; Li, Y. Au-ZnO hybrid nanopyramids and their photocatalytic properties. *J. Am. Chem. Soc.* **2011**, *133*, 5660–5663. [[CrossRef](#)]
28. He, W.; Kim, H.-K.; Wamer, W.G.; Melka, D.; Callahan, J.H.; Yin, J.-J. Photogenerated charge carriers and reactive oxygen species in ZnO/Au hybrid nanostructures with enhanced photocatalytic and antibacterial activity. *J. Am. Chem. Soc.* **2014**, *136*, 750–757. [[CrossRef](#)]
29. Rabanal, M.E. Solvothermal synthesis of Ag/ZnO and Pt/ZnO nanocomposites and comparison of their photocatalytic behaviors on dyes degradation. *Adv. Powder Technol.* **2016**, *27*, 983–993. [[CrossRef](#)]
30. Gupta, J.; Mohapatra, J.; Bahadur, D. Visible light driven mesoporous Ag-embedded ZnO nanocomposites: Reactive oxygen species enhanced photocatalysis, bacterial inhibition and photodynamic therapy. *Dalt. Trans.* **2017**, *46*, 685–696. [[CrossRef](#)]
31. Putri, N.A.; Fauzia, V.; Iwan, S.; Roza, L.; Umar, A.A.; Budi, S. Mn-doping-induced photocatalytic activity enhancement of ZnO nanorods prepared on glass substrates. *Appl. Surf. Sci.* **2018**, *439*, 285–297. [[CrossRef](#)]

32. Kong, J.-Z.; Zhai, H.-F.; Zhang, W.; Wang, S.-S.; Zhao, X.-R.; Li, M.; Li, H.; Li, A.-D.; Wu, D. Visible light-driven photocatalytic performance of N-doped ZnO/g-C₃N₄ Nanocomposites. *Nanoscale Res. Lett.* **2017**. [[CrossRef](#)] [[PubMed](#)]
33. Waiskopf, N.; Ben-Shahar, Y.; Banin, U. Photocatalytic hybrid semiconductor–metal nanoparticles; from synergistic properties to emerging applications. *Adv. Mater.* **2018**, *30*, 1–10. [[CrossRef](#)] [[PubMed](#)]
34. Picciolini, S.; Castagnetti, N.; Vanna, R.; Mehn, D.; Bedoni, M.; Gramatica, F.; Villani, M.; Calestani, D.; Pavesi, M.; Lazzarini, L.; et al. Branched gold nanoparticles on ZnO 3D architecture as biomedical SERS sensors. *RSC Adv.* **2015**, *5*, 93644–93651. [[CrossRef](#)]
35. Zhang, W.; Wang, W.; Shi, H.; Liang, Y.; Fu, J.; Zhu, M. Surface plasmon-driven photoelectrochemical water splitting of aligned ZnO nanorod arrays decorated with loading-controllable Au nanoparticles. *Sol. Energy Mater. Sol. Cells* **2018**, *180*, 25–33. [[CrossRef](#)]
36. Cheng, Y.; Jiao, W.; Li, Q.; Zhang, Y.; Li, S.; Li, D.; Che, R. Two hybrid Au-ZnO aggregates with different hierarchical structures: A comparable study in photocatalysis. *J. Colloid Interface Sci.* **2017**, *509*, 58–67. [[CrossRef](#)]
37. Muravitskaya, A.; Rumyantseva, A.; Kostcheev, S.; Dzhagan, V.; Stroyuk, O.; Adam, P.-M. Enhanced raman scattering of ZnO nanocrystals in the vicinity of gold and silver nanostructured surfaces. *Opt. Express* **2016**, *24*, A168–A173. [[CrossRef](#)]
38. Xie, W.; Li, Y.; Sun, W.; Huang, J.; Xie, H.; Zhao, X. Surface modification of ZnO with Ag improves its photocatalytic efficiency and photostability. *J. Photochem. Photobiol. A Chem.* **2010**, *216*, 149–155. [[CrossRef](#)]
39. Akira, M.; Yanzhi, R.; Kimihiro, M.; Hiroshi, I.; Yukio, M.; Isao, N.; Yukihiko, O. Two-dimensional fourier-transform raman and near-infrared correlation spectroscopy studies of poly(methyl methacrylate) blends: 1. Immiscible blends of poly(methyl methacrylate) and atactic polystyrene. *Vib. Spectrosc.* **2000**, *24*, 171–180.
40. Rumyantseva, A.; Kostcheev, S.; Adam, P.M.; Gaponenko, S.V.; Vaschenko, S.V.; Kulakovich, O.S.; Ramanenka, A.A.; Guzatov, D.V.; Korbutyak, D.; Dzhagan, V.; et al. Nonresonant surface-enhanced raman scattering of ZnO quantum dots with Au and Ag nanoparticles. *ACS Nano* **2013**, *7*, 3420–3426. [[CrossRef](#)]
41. Antony, A.; Poornesh, P.; Kityk, I.V.; Ozga, K.; Jedryka, J.; Philip, R.; Sanjeev, G.; Petwal, V.C.; Verma, V.P.; Dwivedi, J. Methodical engineering of defects in Mn X Zn 1-X O (x = 0.03, and 0.05) nanostructures by electron beam for nonlinear optical applications: A new insight. *Ceram. Int.* **2019**, *45*, 8988–8999. [[CrossRef](#)]
42. Milekhin, A.G.; Sveshnikova, L.L.; Duda, T.A.; Yeryukov, N.A.; Rodyakina, E.E.; Gutakovskii, A.K.; Batsanov, S.A.; Latyshev, A.V.; Zahn, D.R.T. Surface-enhanced Raman spectroscopy of semiconductor nanostructures. *Phys. E Low Dimensional Syst. Nanostruct.* **2016**, *75*, 210–222. [[CrossRef](#)]
43. Barrios-Estrada, C.; de Jesús Rostro-Alanis, M.; Muñoz-Gutiérrez, B.D.; Iqbal, H.M.N.; Kannan, S.; Parra-Saldívar, R. Emergent contaminants: Endocrine disruptors and their laccase-assisted degradation—A review. *Sci. Total Environ.* **2018**, *612*, 1516–1531. [[CrossRef](#)] [[PubMed](#)]
44. Bilic, A.; Reimers, J.R.; Hush, N.S.; Hoft, R.C.; Ford, M.J.; Biosciences, M. Adsorption of benzene on copper, silver, and gold surfaces. *Adsorpt. J. Int. Adsorpt. Soc.* **2006**, *2*, 1093–1105.
45. Ide, Y.; Matsuoka, M.; Ogawa, M. Efficient visible-light-induced photocatalytic activity on gold-nanoparticle-supported layered titanate. *J. Am. Chem. Soc.* **2010**, *132*, 16762–16764. [[CrossRef](#)]
46. Kong, L.; Jiang, Z.; Lai, H.H.; Xiao, T.; Edwards, P.P. Progress in natural science: Materials international does noble metal modi fi cation improve the photocatalytic activity of BiOCl? *Prog. Nat. Sci. Mater. Int.* **2013**, *23*, 286–293. [[CrossRef](#)]
47. Liu, H.; Hu, Y.; Zhang, Z.; Liu, X.; Jia, H.; Xu, B. Synthesis of spherical Ag/ZnO heterostructural composites with excellent photocatalytic activity under visible light and UV irradiation. *Appl. Surf. Sci.* **2015**, *355*, 644–652. [[CrossRef](#)]
48. Gomes, F.; Lopes, A.; Bednarczyk, K.; Gmurek, M.; Stelmachowski, M.; Id, A.Z.; Quinta-Ferreira, M.E.; Costa, R.; Quinta-ferreira, R.M.; Martins, R.C. Effect of noble metals (Ag, Pd, Pt) Loading over the efficiency of TiO₂ during photocatalytic ozonation on the toxicity of parabens. *ChemEngineering* **2018**, *2*, 4. [[CrossRef](#)]

49. Erjavec, B.; Hudoklin, P.; Perc, K.; Tišler, T.; Dolenc, M.S.; Pintar, A. Glass fiber-supported TiO₂ photocatalyst: Efficient mineralization and removal of toxicity/estrogenicity of bisphenol A and its analogs. *Appl. Catal. B Environ.* **2016**, *183*, 149–158. [[CrossRef](#)]
50. Lee, K.M.; Lai, C.W.; Ngai, K.S.; Juan, J.C. Recent developments of zinc oxide based photocatalyst in water treatment technology: A review. *Water Res.* **2016**, *88*, 428–448. [[CrossRef](#)]



© 2019 by the authors. Licensee MDPI, Basel, Switzerland. This article is an open access article distributed under the terms and conditions of the Creative Commons Attribution (CC BY) license (<http://creativecommons.org/licenses/by/4.0/>).